Multi-Linear 3D Craniofacial Infant Shape Model

Till N. Schnabel[1], Yoriko Lill[2,3], Benito K. Benitez[2,3], Gaspard Krief[1], Sebastián Tapia Corón[2,3], Friederike Prüfer[4], Philipp Metzler[5,6], Andreas A. Mueller[2,3], Markus Gross[1], and Barbara Solenthaler[1]

[1] Department of Computer Science, ETH Zurich, Switzerland
till.schnabel@inf.ethz.ch
[2] Oral and Craniomaxillofacial Surgery, University Hospital Basel and University Children's Hospital Basel, Switzerland
[3] Facial and Cranial Anomalies Research Group, Department of Clinical Research and Department of Biomedical Engineering, University of Basel, Switzerland
[4] Department of Radiology, University Children's Hospital Basel, Switzerland
[5] Clinic for Oral and Maxillofacial Surgery, Cantonal Hospital Aarau, Switzerland
[6] Center for Dental Medicine, University of Zurich, Switzerland

Abstract. After birth, the cranium and facial skeleton undergo rapid growth. Routine postnatal assessment is crucial for the early identification of craniofacial deformities, often characterized by asymmetric growth patterns. However, a comprehensive 3D shape model capturing both soft tissue and bony structures during early craniofacial development does not yet exist. We introduce the first integrated 3D shape model of the infant head and skull, constructed from a large dataset of photogrammetric scans complemented by a smaller set of computed tomography scans. Our INfant CRANial (INCRAN) model captures detailed facial expressions and overall cranial shape variations, incorporating the most advanced representation of cranial sutures on the underlying skull to date. By mapping cranial measurements to the model's latent space, we further distinguish various craniofacial deformities from normal shape variations, enabling automated diagnosis and correction proposals. Additionally, we propose a novel method for constructing a multi-linear model from an uncontrolled expression space by projecting an autoencoder back into PCA space, thus enhancing model interpretability. INCRAN supports growth monitoring and holds potential for improving infant healthcare and craniofacial treatment strategies.

Keywords: 3D Infant Cranium · Morphable Shape Model · Malformation Correction · Multi-linear Model

1 Introduction

Routine postnatal assessment of cranial and facial growth is essential for early detection of abnormalities. Craniofacial deformities are characterized by asymmetric growth, most commonly due to positional head deformities. These must be carefully distinguished from the more severe craniosynostosis to ensure accurate diagnosis and appropriate management [20]. While traditional assessments

primarily rely on two-dimensional cranial measurements, recent research suggests that volumetric comparisons enabled by three-dimensional (3D) scans provide a more comprehensive analytical framework [19]. However, manual 3D analysis can be labor-intensive and complex to implement in clinical routine, and treatment planning remains highly subjective. 3D morphable shape models [5, 13, 7] provide a compact representation of complex 3D shape variations, thus enabling detailed and more objective analyses of cranial structures. While several high-quality full-head and skull models have been developed for adults [1, 17], research on the infant cranium remains limited, with only a few models focusing solely on the skull [14, 25, 15] or on the soft-tissue cranium [26, 21, 8], and, to the best of our knowledge, just one model specifically addressing the infant mandible [16].

Our INfant CRANial (INCRAN) model is the first to combine the infant skull, mandible, and soft-tissue cranium, thus capturing important correlations between these domains, including the fusion of important sutures. Moreover, our common mesh topology was designed to perform the common medical measurements mentioned above in an automated fashion and linearly correlating them with the PCA space, thus allowing for continuous cranial shape variation and correction, facilitating planning for possible treatments. Lastly, we present a new method to build a multi-linear PCA model from an uncontrolled expression space, using a linear autoencoder that is reprojected to disentangled PCA spaces after training, making INCRAN the most expressive, complete, and interpretable infant cranial shape model to date. In summary, our main contributions are:

- The first 3D shape model to combine the infant head and skull, which will be made accessible for research purposes.
- The first skull model to capture the course and fusion of all major cranial sutures while combining the cranium with the mandible.
- A multi-linear head model that increases interpretability compared to previous infant models by disentangling identity, expression, and time.
- Discussion of potential medical applications, including growth analysis, skull inference, and a diagnosis and correction of several cranial malformations.

2 Methodology

We begin by discussing the datasets and the registration process used to align the data before applying PCA for dimensionality reduction. We then describe our use of linear regression to join head and skull shape spaces, and to additionally correlate cranial attributes. Finally, we present our method for constructing a multi-linear PCA model from an uncontrolled expression space.

2.1 Data Acquisition and Processing

From the University Hospital Basel and Cantonal Hospital Aarau, we collected and labeled a dataset of 2381 full-head photo scans of 829 different infants aged 8 ± 6 months, primarily undergoing helmet therapy for positional plagiocephaly

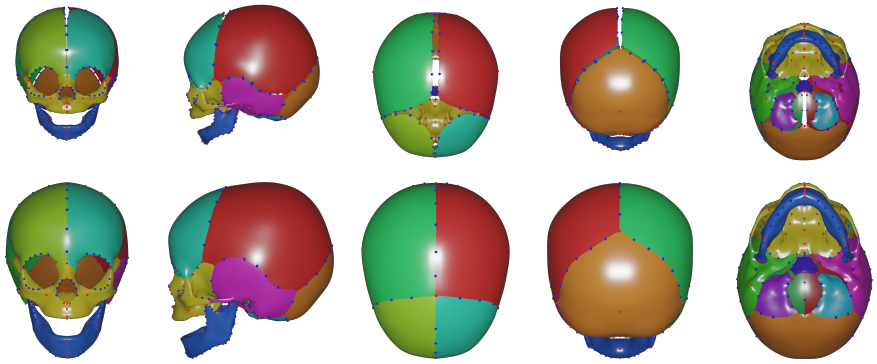

Fig. 1: Five different views of our average skull model (top younger, bottom older) are visualized, demonstrating the age-related fusion of the fontanelle and other important sutures. The coloring highlights disconnected mesh components, and the spheres represent landmarks in red and curvilinear feature points in blue.

or brachycephaly [11]. Scans were acquired using the Vectra M5 scanner, which computes a textured triangular mesh from five simultaneously captured images – two frontal, two posterior, and one top-down. Each mesh was annotated with up to 50 landmarks and 78 curvilinear feature points, along with segmentation of erroneous regions to be excluded from registration [22]. To ensure consistent and interpretable correspondence across all meshes, we applied an extended nonrigid iterative closest point (NICP) algorithm [2]. In addition to registering facial landmarks, a subset of featureless scalp points was aligned to planes defined by the nasion and two tragus points [24]. During each NICP iteration, these points were weighted more heavily to constrain them to their respective planes, enabling automated cranial symmetry and volume distribution measurements on all registered meshes. The ears were generally excluded due to incomplete scanner capture. We refer to this initial set of registered head meshes as $\mathcal{V}_{\text{init}}$.

Additionally, we retrospectively obtained 117 CT scans of infants aged 19±12 months from the database of the University Children's Hospital Basel. Most scans were conducted for suspected head trauma but were later deemed healthy, while the remaining 6 cases involved craniosynostosis. Both the photo and CT datasets maintain equal gender distribution, with a strong predominance of Caucasian ethnicity. CT volumes were converted into triangular surface meshes via automatic density thresholding with manual refinements. Soft tissue meshes were labeled similarly to the photo scans, whereas skull meshes were annotated with up to 134 landmarks and 226 curvilinear feature points. Given that certain cranial sutures remain open for months or years post-birth, these labels trace all major sutures, marking their course along opposing borders [14]. The skull template, designed by an artist and registered via NICP, consists of multiple disconnected components that deform independently to align with each suture's boundary. For fused sutures, adjacent component boundaries were constrained

with fully stiff virtual edges, while for open sutures, boundary points were drawn to a cubic-spline interpolation between corresponding suture border landmarks. The skull template, along with its disconnected components and labels, is visualized in Figure 1, and further animations of its registration process are illustrated in our supplementary video. We refer to the initial set of registered head and skull pairs from this CT dataset as $\mathcal{C}^h_{\text{init}}$ and $\mathcal{C}^s_{\text{init}}$, respectively.

2.2 3D Head-Skull Model

After registration, head and skull mesh pairs from the CT dataset $\{\mathcal{C}^h_{\text{init}}, \mathcal{C}^s_{\text{init}}\}$ undergo joint alignment via generalized Procrustes analysis [10] to the soft-tissue scalp on the template, serving as a rigid reference. The aligned meshes are compressed via PCA, which is used to fill missing regions [3], thus improving alignment between bone and soft tissue. This alignment, model construction, and region filling process iterates until convergence, producing an adjusted set of registered head and skull meshes $\{\mathcal{C}^h, \mathcal{C}^s\}$. The same procedure is applied separately to the photo dataset $\mathcal{V}_{\text{init}}$, yielding $\mathcal{V}$. With all meshes aligned and filled, we construct a head PCA model $P_{\mathcal{H}}$ from the combined head dataset $\mathcal{H} = \mathcal{C}^h \cup \mathcal{V}$, and a separate skull PCA model $P_{\mathcal{C}^s}$ from $\mathcal{C}^s$. We refer to $P_{\mathcal{H}}$ and $P_{\mathcal{C}^s}$ collectively as INCRAN. We selected PCA over a nonlinear model for its robustness with small datasets like $\mathcal{C}^s$ and its interpretability from orthogonality and variance sorting. Moreover, PCA enables training two linear regressors

$$\hat{f}_s : P_{\mathcal{H}} \to P_{\mathcal{C}^s},\ \boldsymbol{z}_h \mapsto \boldsymbol{z}_s, \tag{1}$$

$$\hat{f}_h : P_{\mathcal{C}^s} \to P_{\mathcal{H}},\ \boldsymbol{z}_s \mapsto \boldsymbol{z}_h, \tag{2}$$

to capture head-skull correlations using PCA head projections $\boldsymbol{z}_h$ from $\mathcal{C}^h$ and corresponding paired skull projections $\boldsymbol{z}_s$ from $\mathcal{C}^s$ [6]. Additional linear regressors

$$\hat{f}_{l_i} : P_{\mathcal{H}} \to \mathbb{R},\ \boldsymbol{z}_h \mapsto \boldsymbol{w}_{l_i}^\top (\boldsymbol{z}_h - \bar{\boldsymbol{z}}_h) \approx l_i \tag{3}$$

are trained to determine the direction $\boldsymbol{w}_{l_i}$ of maximum correlation between the PCA vectors $\boldsymbol{z}_h$ and several important attributes l_i, similar to prior work [23, 21, 8], allowing this specific attribute to be varied by changing $\boldsymbol{z}_h$ along $\boldsymbol{w}_{l_i}$.

2.3 Linear Disentanglement

In [22], the first infant morphable model was introduced to disentangle identity and expression spaces with a nonlinear autoencoder, addressing challenges from uncontrolled infant expressions with a training scheme proposed by [28]. The authors further leveraged longitudinal data to isolate a single-component age space. We adopt this approach to enhance INCRAN's interpretability but introduce two key modifications: First, instead of a single-component age space, we allow multiple components, enabling the model to capture variations beyond average aging, such as treatment-induced head cranial shape corrections or weight fluctuations. Second, we use a linear autoencoder to maintain compatibility with the linear

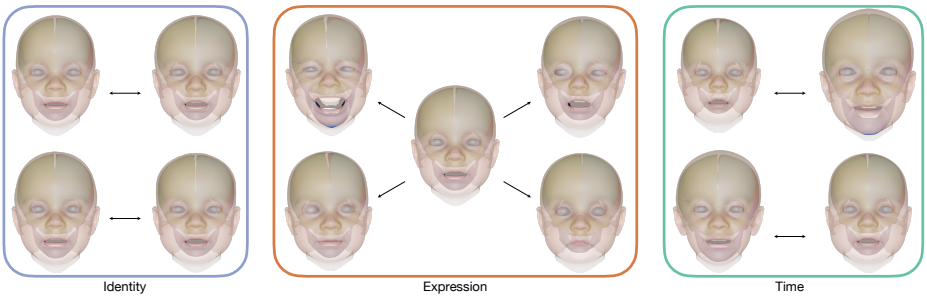

Fig. 2: For each disentangled space, variations along the first two components are shown on opposite arrow sides. The average cranium is shown in the center.

regressors from (1), (2), and (3). Additionally, [12] demonstrated that linear autoencoders trained with L_2 reconstruction loss and weight regularization can be transformed back into a PCA-like space via singular value decomposition, which restores PCA's advantages of orthogonality and variance sorting post-training, preserving interpretability. Formally, we define the disentangled autoencoder

$$\mathcal{F}(\boldsymbol{x}_h) = g_\beta(f_\beta(\boldsymbol{x}_h)) + g_\gamma(f_\gamma(\boldsymbol{x}_h)) + g_\alpha(f_\alpha(\boldsymbol{x}_h)) \tag{4}$$

as a sum of three separate linear autoencoders $g_\beta(f_\beta), g_\gamma(f_\gamma), g_\alpha(f_\alpha)$ for modeling identity-, expression-, and time-related factors, respectively. These autoencoders are trained jointly in an end-to-end manner, using batches of quadruplets where each element captures controlled variations across the three disentangled factors [22]. Each encoder $f_{j\in\{\beta,\gamma,\alpha\}}$ applies a linear transformation $\mathbf{W}_1^j \in \mathbb{R}^{d\times p_j}$ to the input vector $\boldsymbol{x}_h \in \mathbb{R}^d$, generating a compact p_j-dimensional representation, which the decoder multiplies with $\mathbf{W}_2^j \in \mathbb{R}^{p_j\times d}$ to reconstruct the input. To remove potential correlations between the three spaces, we project each matrix into the orthogonal complement of the other two: $\mathbf{W}_2^{j'} = \mathbf{W}_2^j \cap \left(\mathbf{W}_2^k + \mathbf{W}_2^l\right)^\perp$. Each projected matrix is then reparametrized using thin SVD: $\mathbf{W}_2^{j'} = \mathbf{U}^j\mathbf{\Sigma}^j\mathbf{V}^{j\top}$, producing orthogonal weight matrices $\mathbf{U}^j \in \mathbb{R}^{p_j\times d}$ with columns sorted by variance. The final multi-linear PCA-like model $P_\mathcal{H}^+$ is obtained by combining these reparametrized decoder matrices into the projection matrix $\mathbf{U} = \left[\mathbf{U}^\beta, \mathbf{U}^\gamma, \mathbf{U}^\alpha\right]$. $P_\mathcal{H}^+$ is trained exclusively on the head dataset $\mathcal{H}$, as the skull dataset $\mathcal{C}^s$ is too small for training a neural network and lacks intra-subject scans, which are crucial for disentanglement. However, by correlating the skull and soft-tissue domains via (1), the disentanglement effectively transfers to the skull. Figure 2 illustrates the variations encoded in these three spaces, including growth and weight fluctuations in the time space, additionally rendering the coupled skull below the soft-tissue surface.

3 Results and Applications

We evaluate INCRAN's performance before exploring its potential applications.

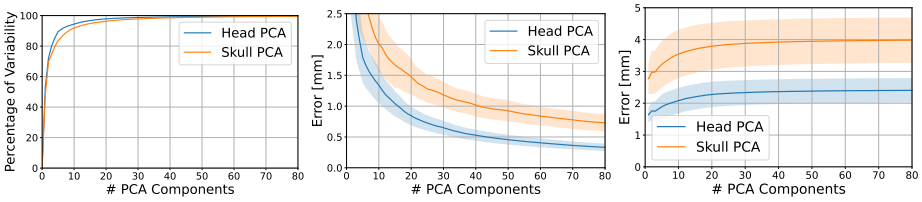

Fig. 3: Model compactness (left), generalization (center), and specificity (right).

3.1 Model Training and Evaluation

Figure 3 evaluates compactness, generalization, and specificity [13] for the single-space PCA models of the head ($P_{\mathcal{H}}$) and skull ($P_{\mathcal{C}^s}$), where errors between two meshes were calculated as the average euclidean distance between corresponding vertex pairs. Both models were trained on the full dataset for compactness and specificity, while generalization was assessed via 10-fold cross-validation. As expected, $P_{\mathcal{H}}$ outperforms $P_{\mathcal{C}^s}$ in generalization and specificity, with comparable compactness, due to the substantially larger dataset size. For further analysis, we limit both models to 64 components, preserving approximately 99.5 % of the total variance. In the multi-linear model, $P^+_{\mathcal{H}}$, the dimensionality of each disentangled subspace was determined experimentally from the eigenvalues of $\mathbf{\Sigma}^j$, resulting in 8 components for identity, 32 for expression, and 16 for time. $P^+_{\mathcal{H}}$ was trained on $\mathcal{H}$ with a 90/10 train-validation split with the same scheme as in [22], except for using L_2 as reconstruction loss and weight regularization. Additionally, early stopping was applied after 300 iterations when the L_2 weight norm reached its minimum, as continued training led to a further decrease in reconstruction loss but an increase in the weight norm, which resulted in visual degradation of the orthogonal latent features $\mathbf{U}$. Consequently, $P^+_{\mathcal{H}}$ exhibits a notable accuracy loss (0.52 ± 0.11 mm) compared to the uniform PCA model $P_{\mathcal{H}}$ (0.44 ± 0.08 mm). Moreover, it does not perfectly separate identity, expression, and time. For instance, the expression space captures scalp movement, as demonstrated in our supplementary video, due to the scan-wise registration process, which does not consider intra-subject correlations. We suspect this contributes to the relatively low variance allocated to the identity space.

3.2 Growth Analysis

Training the linear regressor from (3) to predict a baby's age yields a mean absolute error of 2.1 ± 4.7 months on $\mathcal{V}$, improving upon the mean-age baseline error of 3.2 ± 5.4 months. On $\mathcal{C}^h$, it achieves 4.5 ± 3.3 months, which further improves to 3.6 ± 3.0 months when incorporating $\mathcal{C}^h$, compared to 7.3 ± 5.1 months for the mean-age baseline. Although the age distribution in $\mathcal{V}$ is smaller and narrower than in $\mathcal{C}^h$ (8 ± 6 vs. 19 ± 12 months), the predictions still exhibit a larger standard deviation, potentially because a linear approximation of nonlinear growth is less accurate for younger infants who grow more rapidly [15]. The improved

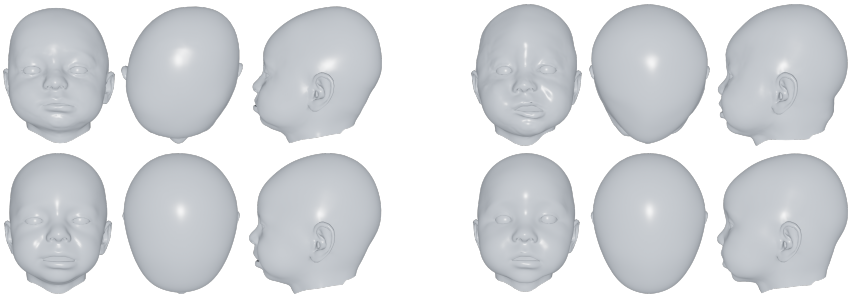

Fig. 4: Our model detects in the input (top) and corrects (bottom) positional plagiocephaly (left) and metopic suture craniosynostosis (right).

accuracy when incorporating the skull data from $\mathcal{C}^s$ aligns with prior research showing that skull sutures serve as reliable age indicators [18], as visualized in Figure 1, where the age is varied in the skull PCA space along $\boldsymbol{w}_{l_i}$, thus showing the fusion of the fontanelle and other important sutures. The prediction and variation of age via our model shows potential to make infant growth analysis more objective and comprehensive. By quantifying 3D cranial development, our approach supports routine growth monitoring and may help detect deviations from normative growth trajectories at an early stage. This could prove valuable in identifying conditions such as craniosynostosis or neurodevelopmental disorders, where cranial morphology is affected, at an early stage. Furthermore, INCRAN may support longitudinal tracking of post-surgical outcomes or the evaluation of therapeutic interventions in infants with diagnosed growth anomalies.

3.3 Diagnosis and Correction of Craniofacial Malformations

We computed key cranial measurements commonly used to assess abnormal skull shapes [19] across the entire dataset $\mathcal{H}$ and trained linear regressors from (3) for each. Notably, these measurements correlate most strongly with the time space of the disentangled model $P^+_{\mathcal{H}}$, likely because most subjects with longitudinal data underwent treatment for cranial shape correction. The regressors enable automatic prediction of these measurements for new patients, facilitating anomaly detection and potentially enabling more objective diagnoses of cranial malformations. Furthermore, the regressors can be used to adjust cranial shapes to bring any specific or all measurements combined into a healthy range. Figure 4 illustrates this process for infants with craniosynostosis and positional plagiocephaly. Our approach differs from prior work [21, 8] in that it does not apply binary classification to detect and correct only craniosynostosis, but rather regresses these key cranial measurements to represent and correct any type of cranial malformation in a continuous fashion. The corrected cranium could serve as a healthy reference for clinicians, aiding treatment planning. By also fixing the estimated age and total cranial volume, we simulate potential treatment interventions for cranial deformities. For non-surgical treatments, such as helmet therapy [11],

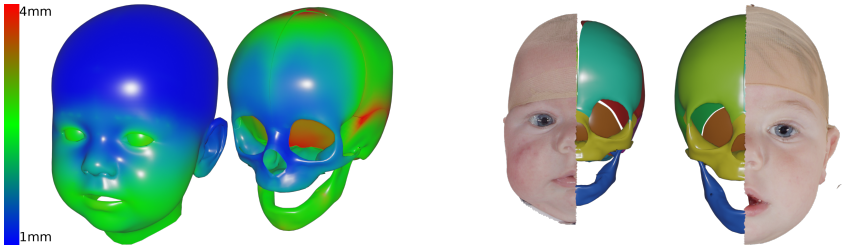

Fig. 5: Left highlights the regional accuracy of face and skull inference, averaged over the CT dataset. Right demonstrates skull inference on non-invasive photo scans for the same baby at three and eleven months.

patient growth could be imitated by incrementally increasing the age direction and constraining specific head regions while allowing others to develop naturally.

3.4 Face and Skull Inference

Facial reconstruction from skulls is crucial for forensic applications, and INCRAN extends previous analyses limited to adults [9, 17]. Using (2), we achieve a vertex reconstruction error of 1.8 ± 1.1 mm via ridge regression. Conversely, our model infers skull structures from soft tissue using (1) with an accuracy of 2.7 ± 1.6 mm. Figure 5 visualizes the inference error distribution, which is most pronounced at the sutures, likely due to PCA's linear approximation of their nonlinear growth pattern. Skull inference presents a valuable tool for craniofacial malformation diagnosis and treatment, addressing the challenges of routine skull monitoring, which is limited by the risks associated with radiation exposure. By enhancing photogrammetric analysis, it enables noninvasive and clinically informative monitoring of craniofacial growths, as demonstrated in Figure 5.

4 Discussion and Conclusion

We presented INCRAN, the most comprehensive infant craniofacial shape model to date, encompassing the skull, mandible, and soft-tissue cranium, featuring detailed modeling of all major sutures. Additionally, we proposed a novel approach to constructing a multi-linear PCA model by reprojecting the latent space of an autoencoder trained to iteratively disentangle identity, expression, and time variations. Finally, we demonstrated potential medical applications, including automatic diagnosis and correction planning for craniofacial malformations. Future work should focus on increasing dataset diversity to mitigate racial bias. Additionally, expanding the CT dataset, particularly with malformed cases, could reduce domain shifts between our two datasets and improve precision of the domain regressors $\hat{f}_s, \hat{f}_h$, especially in predicting premature suture fusion in craniosynostosis. With more data, automated labeling methods [27,

8, 4] should be explored, and nonlinear models could further refine the encoding of cranial growth, including closure of the sutures. Moreover, model-based registration [13] could enhance intra-subject alignment and thus improve the disentanglement of identity and expression. However, the challenge of defining a comprehensive identity space, independent of time-related changes, may stem from a deeper underlying question. We leave the reader to reflect on what truly constitutes identity, if not its present state in time.

Acknowledgments. Funding was provided by the Swiss National Science Foundation (Grant No. 205321_205008) and by the Botnar Research Centre for Child Health. The collection and further use of the clinical data received the IRB approval by Ethikkommission Nordwest- und Zentralschweiz (EKNZ) on February 25th, 2021 (Protocol No. 2021-00327). We thank Defne Kurtulus and Baran Gözcü for their contributions during Defne's Bachelor's thesis, Doriano van Essen for his design of the skull template, and Olivia Williams for her labeling efforts. We further thank the parents for giving their consent for the use of the image material presented in Figures 4 and 5.

Disclosure of Interests. The authors have no competing interests to declare that are relevant to the content of this article.

References

1. Achenbach, J., Brylka, R., Gietzen, T., Hebel, K.z., Schömer, E., Schulze, R., Botsch, M., Schwanecke, U.: A Multilinear Model for Bidirectional Craniofacial Reconstruction. In: Puig Puig, A., Schultz, T., Vilanova, A., Hotz, I., Kozlikova, B., Vázquez, P.P. (eds.) Eurographics Workshop on Visual Computing for Biology and Medicine. The Eurographics Association (2018). https://doi.org/10.2312/vcbm.20181230
2. Amberg, B., Romdhani, S., Vetter, T.: Optimal step nonrigid icp algorithms for surface registration. In: IEEE Conf Comput Vis Pattern Recognit (CVPR). pp. 1–8 (2007). https://doi.org/10.1109/CVPR.2007.383165
3. Basso, C., Vetter, T.: Statistically motivated 3d faces reconstruction. In: Proceedings of the 2nd international conference on reconstruction of soft facial parts. vol. 31. Citeseer (2005)
4. Bhalodia, R., Elhabian, S., Adams, J., Tao, W., Kavan, L., Whitaker, R.: Deepssm: A blueprint for image-to-shape deep learning models. Medical Image Analysis **91**, 103034 (2024). https://doi.org/10.1016/j.media.2023.103034
5. Blanz, V., Vetter, T.: A morphable model for the synthesis of 3d faces. In: Proceedings of the 26th Annual Conference on Computer Graphics and Interactive Techniques. p. 187–194. SIGGRAPH '99, ACM Press/Addison-Wesley Publishing Co., USA (1999). https://doi.org/10.1145/311535.311556
6. Duan, F., Huang, D., Tian, Y., Lu, K., Wu, Z., Zhou, M.: 3d face reconstruction from skull by regression modeling in shape parameter spaces. Neurocomputing **151**, 674–682 (2015). https://doi.org/10.1016/j.neucom.2014.04.089
7. Egger, B., Smith, W.A.P., Tewari, A., Wuhrer, S., Zollhoefer, M., Beeler, T., Bernard, F., Bolkart, T., Kortylewski, A., Romdhani, S., Theobalt, C., Blanz, V., Vetter, T.: 3d morphable face models—past, present, and future. ACM Trans. Graph. **39**(5) (2020). https://doi.org/10.1145/3395208

8. Elkhill, C., Liu, J., Linguraru, M.G., LeBeau, S., Khechoyan, D., French, B., Porras, A.R.: Geometric learning and statistical modeling for surgical outcomes evaluation in craniosynostosis using 3d photogrammetry. Computer Methods and Programs in Biomedicine **240**, 107689 (2023). https://doi.org/10.1016/j.cmpb.2023.107689
9. Gietzen, T., Brylka, R., Achenbach, J., zum Hebel, K., Schömer, E., Botsch, M., Schwanecke, U., Schulze, R.: A method for automatic forensic facial reconstruction based on dense statistics of soft tissue thickness. PLoS ONE **14** (1 2019). https://doi.org/10.1371/journal.pone.0210257
10. Gower, J.C.: Generalized procrustes analysis. Psychometrika **40**(1), 33–51 (1975). https://doi.org/10.1007/BF02291478
11. Kropla, F., Hoffmann, M., Winkler, D., Krause, M., Scholz, S., Grunert, R.: Development of an individual helmet orthosis for infants based on a 3d scan. 3D Printing in Medicine **9**(1), 22 (Aug 2023). https://doi.org/10.1186/s41205-023-00187-7
12. Kunin, D., Bloom, J., Goeva, A., Seed, C.: Loss landscapes of regularized linear autoencoders. In: Chaudhuri, K., Salakhutdinov, R. (eds.) Proceedings of the 36th International Conference on Machine Learning. Proceedings of Machine Learning Research, vol. 97, pp. 3560–3569. PMLR (09–15 Jun 2019), https://proceedings.mlr.press/v97/kunin19a.html
13. Li, T., Bolkart, T., Black, M.J., Li, H., Romero, J.: Learning a model of facial shape and expression from 4D scans. ACM Transactions on Graphics, (Proc. SIGGRAPH Asia) **36**(6), 194:1–194:17 (2017). https://doi.org/10.1145/3130800.3130813
14. Li, Z., Park, B.K., Liu, W., Zhang, J., Reed, M.P., Rupp, J.D., Hoff, C.N., Hu, J.: A statistical skull geometry model for children 0-3 years old. PLoS One **10**(5), e0127322 (May 2015). https://doi.org/10.1371/journal.pone.0127322
15. Liang, C., Profico, A., Buzi, C., Khonsari, R.H., Johnson, D., O'Higgins, P., Moazen, M.: Normal human craniofacial growth and development from 0 to 4 years. Scientific Reports **13** (12 2023). https://doi.org/10.1038/s41598-023-36646-8
16. O' Sullivan, E., van de Lande, L.S., El Ghoul, K., Koudstaal, M.J., Schievano, S., Khonsari, R.H., Dunaway, D.J., Zafeiriou, S.: Growth patterns and shape development of the paediatric mandible – a 3d statistical model. Bone Reports **16**, 101528 (2022). https://doi.org/10.1016/j.bonr.2022.101528
17. Qiu, Z., Li, Y., He, D., Zhang, Q., Zhang, L., Zhang, Y., Wang, J., Xu, L., Wang, X., Zhang, Y., Yu, J.: Sculptor: Skeleton-consistent face creation using a learned parametric generator. ACM Transactions on Graphics **41** (11 2022). https://doi.org/10.1145/3550454.3555462
18. Ruengdit, S., Troy Case, D., Mahakkanukrauh, P.: Cranial suture closure as an age indicator: A review. Forensic Science International **307**, 110111 (2020). https://doi.org/10.1016/j.forsciint.2019.110111
19. Santander, P., Quast, A., Hubbert, J., Juenemann, L., Horn, S., Hensel, K.O., Meyer-Marcotty, P., Dieks, J.K.: Stereophotogrammetric head shape assessment in neonates is feasible and can identify distinct differences between term-born and very preterm infants at term equivalent age. Scientific Reports **11** (12 2021). https://doi.org/10.1038/s41598-021-00680-1
20. Santiago, G.S., Santiago, C.N., Chwa, E.S., Purnell, C.A.: Positional plagiocephaly and craniosynostosis. Pediatric annals **52**(1), e10–e17 (2023)
21. Schaufelberger, M., Kühle, R., Wachter, A., Weichel, F., Hagen, N., Ringwald, F., Eisenmann, U., Hoffmann, J., Engel, M., Freudlsperger, C., Nahm, W.: A radiation-free classification pipeline for craniosynostosis using statistical shape modeling. Diagnostics **12**(7) (2022). https://doi.org/10.3390/diagnostics12071516

22. Schnabel, T.N., Lill, Y., Benitez, B.K., Nalabothu, P., Metzler, P., Mueller, A.A., Gross, M., Gözcü, B., Solenthaler, B.: Large-scale 3d infant face model. In: Medical Image Computing and Computer Assisted Intervention – MICCAI 2024. pp. 217–227. Springer Nature Switzerland, Cham (2024). https://doi.org/10.1007/978-3-031-72384-1_21
23. Schumacher, M., Blanz, V.: Exploration of the correlations of attributes and features in faces. In: 2015 11th IEEE International Conference and Workshops on Automatic Face and Gesture Recognition (FG). vol. 1, pp. 1–8 (2015). https://doi.org/10.1109/FG.2015.7163124
24. Schweitzer, T., Böhm, H., Linz, C., Jager, B., Gerstl, L., Kunz, F., Stellzig-Eisenhauer, A., Ernestus, R.I., Krauß, J., Meyer-Marcotty, P.: Three-dimensional analysis of positional plagiocephaly before and after molding helmet therapy in comparison to normal head growth. Child's Nervous System **29**(7), 1155–1161 (Jul 2013). https://doi.org/10.1007/s00381-013-2030-y
25. Sullivan, E.O., van de Lande, L.S., Oosting, A.J.C., Papaioannou, A., Jeelani, N.O., Koudstaal, M.J., Khonsari, R.H., Dunaway, D.J., Zafeiriou, S., Schievano, S.: The 3d skull 0–4 years: A validated, generative, statistical shape model. Bone Reports **15** (12 2021). https://doi.org/10.1016/j.bonr.2021.101154
26. Torres, H.R., Oliveira, B., Morais, P., Fritze, A., Rüdiger, M., Fonseca, J.C., Vilaça, J.L.: Realistic 3d infant head surfaces augmentation to improve ai-based diagnosis of cranial deformities. Journal of Biomedical Informatics **132**, 104121 (8 2022). https://doi.org/10.1016/J.JBI.2022.104121
27. Torres, H.R., Oliveira, B., Veloso, F., Ruediger, M., Burkhardt, W., Moreira, A., Dias, N., Morais, P., Fonseca, J.C., Vilaça, J.L.: Deep learning-based detection of anthropometric landmarks in 3d infants head models. In: Medical Imaging 2019: Computer-Aided Diagnosis. vol. 10950, pp. 791–797. SPIE (2019). https://doi.org/10.1117/12.2512196
28. Zhou, K., Bhatnagar, B.L., Pons-Moll, G.: Unsupervised shape and pose disentanglement for 3d meshes. In: Vedaldi, A., Bischof, H., Brox, T., Frahm, J.M. (eds.) Computer Vision – ECCV 2020. pp. 341–357. Springer International Publishing, Cham (2020). https://doi.org/10.1007/978-3-030-58542-6_21